Nanoscale Advances

ROYAL SOCIETY OF CHEMISTRY

PAPER

View Article Online
View Journal

Cite this: DOI: 10.1039/d5na00915d

Computationally validated magnesium and graphene oxide anchored SnO_2 quantum dots for RhB reduction and antibacterial activity

Eman Rai,[a] Muhammad Imran,*[b] Iram Shahzadi,[c] Ali Haider,*[d] Sawaira Moeen,[ef] Anwar Ul-Hamid,[g] I Boukhris[h] and Muhammad Ikram*[ef]

Developing multi-functional catalysts for wastewater purification and bactericidal inactivation is quite interesting but remains a significant challenge. Herein, varying concentrations (2 and 4 wt%) of magnesium (Mg) doped with a fixed amount of graphene oxide–stannic oxide quantum dots (GO–SnO_2 QDs) were prepared by a low temperature co-precipitation approach. This research provides dual approaches, experimental as well as theoretical, to study the properties of doping-dependent SnO_2 for rhodamine B degradation and MDR *S. aureus* inactivation. The addition of two-dimensional GO exposed more active sites, and Mg metal facilitates the transportation of charge carriers for catalytic and antibacterial activity. Advanced characterization confirmed the multiple phases (tetragonal, orthorhombic, and anorthic), polycrystalline behavior, high light absorption intensity, and the QD-like morphology of ternary catalysts. The combination of metal, 2D materials, and metal oxides was proven to be beneficial as they synergistically increased the catalytic activities. Among all synthesized samples, optimized 4% Mg/GO–SnO_2 revealed considerable (94.7%) rhodamine B (RhB) degradation in acidic medium. The optimized sample exhibited a 3.65 ± 0.03 mm inhibition zone towards MDR *S. aureus* in comparison to ciprofloxacin. Mg/GO-doped SnO_2 exhibited significant inhibitory effects on DNA gyrase and tyrosyl-tRNA synthetase (TyrRS), as corroborated by the *in silico* approach, indicating its potential as a therapeutic agent for bactericidal action.

Received 25th September 2025
Accepted 16th March 2026

DOI: 10.1039/d5na00915d

rsc.li/nanoscale-advances

1 Introduction

Organic dyes and other potentially hazardous substances are released by industries into freshwater reservoirs, which exhibit complex detrimental impacts on aquatic ecosystems.[1] The effluent of hazardous chemicals by textile manufacturers contributes significantly towards the detrimental impacts on the ecosystem and human wellness.[2] RhB is a cationic, extremely water-soluble dye that induces thyroid damage, allergic dermatitis, and adverse respiratory effects.[3–5] Additionally, bovine mastitis is a particularly prevalent disease affecting dairy cows worldwide. The illness is multifactorial, caused by various infectious agents, leading to significant economic losses and negative impacts on the dairy industry, characterized by decreased milk yield and heightened culling and treatment costs.[6] *Staphylococcus aureus* (*S. aureus*) is often regarded as a causative agent of infectious mastitis. The excessive use of antibiotics in the treatment of mastitis is the main factor contributing to increased resistance in dairy cows.[7,8] The extensive use of antibiotics poses a considerable risk to human health, primarily through the development of bacterial resistance and the contamination of milk with antibiotic residues. An urgent need exists to develop a novel and safe approach for mastitis treatment that prioritizes public health.[9]

Adsorption, reverse osmosis, and ion exchange are the primary techniques for removing dyes from contaminated water, each offering unique benefits and limitations.[10] In particular, catalytic decomposition has attracted interest as a pragmatic, energy-efficient, and environmentally sustainable approach.[11] In recent decades, semiconductor nanomaterials have attracted considerable attention from researchers in environmental development

[a]*Department of Chemistry, Government College University, Faisalabad, Pakpattan Road, Sahiwal, Punjab, 57000, Pakistan*
[b]*Interdisciplinary Research Center for Hydrogen Technologies and Carbon Management (IRC-HTCM), King Fahd University of Petroleum & Minerals, Dhahran, 31261, Saudi Arabia*
[c]*School of Pharmacy, University of Management and Technology, Lahore, 54770, Pakistan*
[d]*Department of Clinical Sciences, Faculty of Veterinary and Animal Sciences, Muhammad Nawaz Shareef, University of Agriculture, Multan 66000, Punjab, Pakistan. E-mail: ali.haider@mnsuam.edu.pk*
[e]*Solar Cell Applications Research Lab, Department of Physics, Government College University Lahore, Lahore 54000, Punjab, Pakistan*
[f]*Advance Nanomaterials Research Lab (ANRL), Department of Physics, Government College University Lahore, 54000, Lahore, Punjab, Pakistan*
[g]*Core Research Facilities, King Fahd University of Petroleum & Minerals, Dhahran 31261, Saudi Arabia*
[h]*Department of Physics, College of Science, King Khalid University, P. O. Box 9004, Abha, Saudi Arabia*

due to their notable physicochemical properties, especially their reduced toxicity and environmental sustainability.[12] Various methods have been employed to prepare metal oxides, including ZnO (hydrothermal method and nanoflake-like morphology),[13] Al_2O_3 (sol–gel method and nanoparticles),[14] V_2O_5 (ultrasound-assisted synthesis and nanoparticles (NPs)),[15] and SnO_2 (co-precipitation method and NPs).[16] Among these, co-precipitation-synthesized SnO_2 has now been suggested as an efficient catalyst owing to its chemical stability, cost-effectiveness and low toxicity.[17] This method provides economic viability and regulates NP synthesis, surface area, and stoichiometry without needing high-temperature systems.[18–20] Furthermore, SnO_2 is an n-type semiconductor with a wide bandgap energy (E_g), high electron mobility, and low resistivity.[21–24] However, SnO_2 has a rapid e^-/h^+ recombination rate, which limits its application for RhB degradation.[25]

To address this issue, carbon-based nanomaterials such as g-C_3N_4, graphene oxide (GO), and carbon nanotubes were employed due to their chemical stability and high conductivity.[26] GO, a 2D aromatic compound, is considered the best option for improving the catalytic reduction of RhB as well as antibacterial activity due to its biocompatibility, extensive surface area, low E_g and high adsorption capacity.[27] So, we selected GO as a doping agent. The dye reduction efficacy of SnO_2 was further enhanced by doping with metals (Be, Mg, Ca and Sr), as they produce lattice imperfections, including oxygen vacancies and enhanced the formation of reactive oxygen species (ROS).[12]

To our knowledge, no reports have investigated the co-precipitation synthesis of Mg/GO–SnO_2 QDs for catalytic and antibacterial activity.

2 Experimental section

2.1 Materials

$SnCl_2 \cdot 2H_2O$ (purity~99%), graphite powder (99%), $MgCl_2 \cdot 6H_2O$, 99%, sodium nitrate ($NaNO_3$, 99.9%), hydrogen peroxide (H_2O_2), potassium permanganate ($KMnO_4$, 99.5%) and NaOH (99%) were acquired from Sigma Aldrich (Germany) while, H_2SO_4, HCl, and H_3PO_4 were obtained from Analar.

2.2 Synthesis of SnO_2 and Mg/GO–SnO_2

SnO_2 was prepared based on our previous studies with a few characterization results reused (https://doi.org/10.1039/D3RA00698K).[28] The prepared material is named SnO_2 (sample 1) in the subsequent text. Graphene oxide (GO) was prepared by the modified Hummer approach, as reported earlier.[29] GO–SnO_2 was prepared by adding 2 wt% GO in $SnCl_2 \cdot 2H_2O$ solution under the same conditions and this is named GO–SnO_2 (sample 2) in the remaining part of the manuscript. Similarly, ternary catalysts (Mg/GO–SnO_2) were prepared using 2 and 4 wt% Mg in GO/$SnCl_2 \cdot 2H_2O$ solution, keeping the same conditions (Fig. 1) and are referred to as 2 and 4% Mg/GO–SnO_2 (sample no 3 and 4) in the subsequent text.

2.3 Catalytic dye degradation activity

The catalytic RhB reduction efficacy of SnO_2, GO–SnO_2 and Mg/GO–SnO_2 was evaluated in the dark in the presence of a reducing agent ($NaBH_4$). Firstly, 0.1 M $NaBH_4$ was injected into 5 mL RhB solution (5 mg/500 mL) under constant agitation. Subsequently, 400 μL of SnO_2, GO–SnO_2 and Mg/GO–SnO_2 solutions (5 mg/10 mL) were integrated into the above solution, and RhB reduction was recorded using a UV-vis spectrophotometer after specific intervals.

2.4 Segregation and characterization of *S. aureus*

Samples of raw milk were collected from mastitis-positive cows milked at different locations in Punjab, Pakistan, including marketplaces and veterinary facilities. The milk specimens were promptly delivered to the laboratory at 4 °C following collection. The growth potential of *Staphylococcus aureus* (*S. aureus*) in

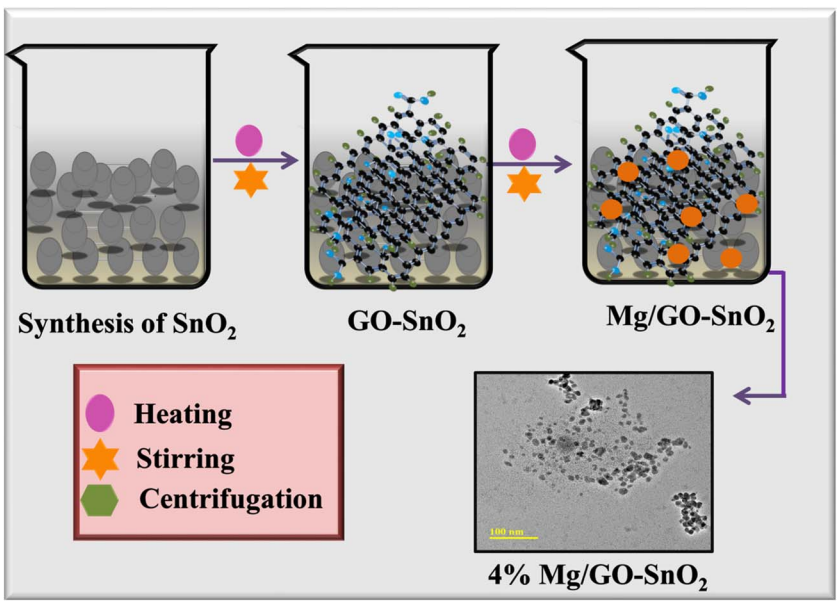

Fig. 1 Schematic preparation of Mg/GO–SnO_2.

unpasteurized milk was evaluated by cultivating specimens thrice on mannitol salt agar (MSA) following aerobic incubation at a specific temperature (37 °C) for 48 hours. The purified culture attained was characterized morphologically and biochemically using Gram staining and different biochemical tests. Furthermore, the susceptibility of isolated *S. aureus* for different antibiotics was analyzed and the resulting bacteria found resistant to at-least three drugs were classified as multiple drug resistant (MDR).[7]

2.4.1 Antibacterial effectiveness. Ten distinct MDR *S. aureus* strains obtained from mastitis milk were assessed for the antibacterial effectiveness of SnO_2, GO–SnO_2 and (2 and 4 wt%) Mg/GO–SnO_2 using the well diffusion approach. Petri dishes containing MSA were swabbed with 0.5 McFarland suspension of MDR *S. aureus*. Control SnO_2 and doped SnO_2 were loaded into 6 mm wells on MSA plates at concentrations of 500 and 1000 μg/50 μL. The positive control treatment (5 μg/50 μL) included ciprofloxacin, while the substitute control was composed of (50 μL) DI water. The extent of inhibition domains was assessed quantitatively utilizing a digital vernier scale after incubation at 37 °C for 24 hours. The statistical validation of quantified inhibition domains (mm) considering a significance level <5% was performed using one way analysis of variance (ANOVA) with SPSS 24.0.

2.5 Molecular docking analysis

A plethora of nanocomposites have shown efficiency in the elimination of bacteria. QDs have been shown to have biological potential, but further study is needed to pinpoint how exactly they exert their therapeutic effects. Researchers from all over the world are now able to undertake in-depth assessments of a wide range of interactions and developments owing to the widespread use of computational approaches, in particular molecular docking studies. In light of the notable antibacterial properties demonstrated by the synthesized nanocomposites, our principal aim in this study was to assess their viability as molecular docking-based inhibitors of specific enzymes. We tested the inhibitory effect of Mg/GO–doped SnO_2 on DNA gyrase and tyrosyl-tRNA synthetase (TyrRS) to establish its potential against *S. aureus*. Crystal structures of DNA $gyrase_{S.\ aureus}$ and $TyrRS_{S.\ aureus}$ (PDB codes 5CTU and 1JIJ; https://www.rcsb.org/) were downloaded from the RCSB PDB. For the docking study, we used the SYBYL-X 2.0 program. To construct 3D models of the compounds of interest and investigate interactions between QDs and active site residues of the proteins of interest, we used the SYBYL-X 2.0 program in the same way as described in our previous paper.[30,31]

3 Results and discussion

The structural properties of SnO_2 and Mg/GO–SnO_2 were characterized by XRD analysis, over a 2θ range of 20 to 70° (Fig. 2a). Peaks at 26.4, 33.7, 37.8, 51.5, 54.5, 61.6, and 65.5 correspond to the tetragonal phase ($P4_2/mnm$, no. 136) of SnO_2, as confirmed by JCPDS card no. 01-077-0452. Other diffraction peaks at 24.9° (111), 29.8° (101), 31.2° (020), 45.4° (024), and 47.0° (115) are ascribed to orthorhombic ($Cmc2_1$, no. 36) and tetragonal phases ($P4/nmm$, no. 129) of SnO (JCPDS card no. 01-077-2296/00-006-0395). Additional peaks at 21.7° (020), 56.3° ($3\bar{1}1$) and 58.6° ($0\bar{3}2$) confirmed the anorthic structure (P^*, no. 2) of Sn_2O_3 (JCPDS card no. 00-025-1259). Compared to the pure sample, the relative peak intensity or crystallinity of GO–SnO_2 decreased owing to various functional groups, including carboxylic acid and hydroxyl.[32,33] With Mg, the crystallinity was further reduced as Mg^{2+} (0.072 nm) has a larger ionic radius compared to Sn^{4+} (0.071 nm).[12] SAED patterns of GO–SnO_2 and 4% Mg/GO–SnO_2, containing identifiable bright rings showing polycrystalline behavior (Fig. 2b and c).

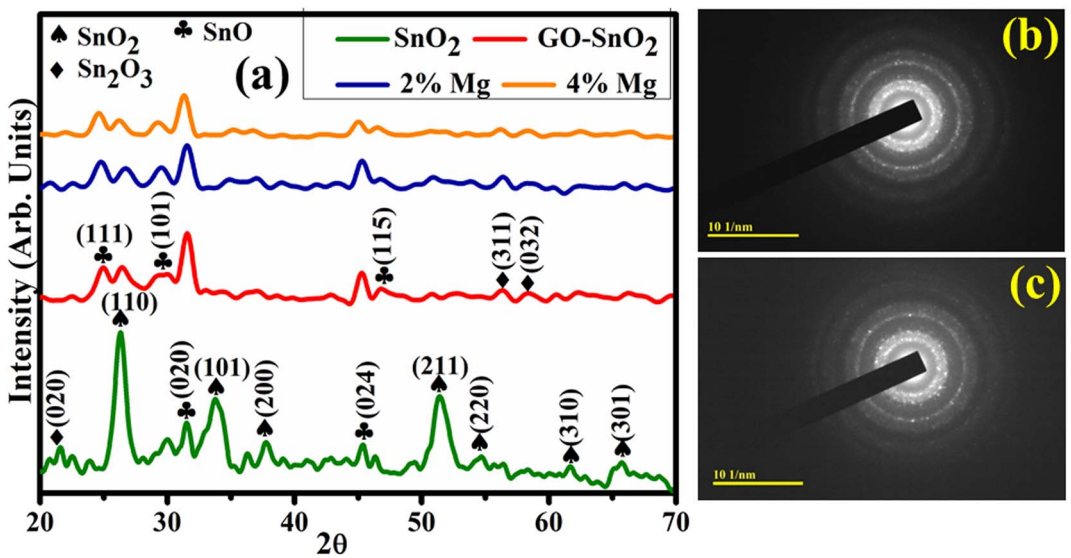

Fig. 2 (a) Diffraction patterns of SnO_2,[34] GO–SnO_2, 2% Mg/GO–SnO_2 and 4% Mg/GO–SnO_2 and (b and c) SAED analysis of GO–SnO_2 and 4% Mg/GO–SnO_2.

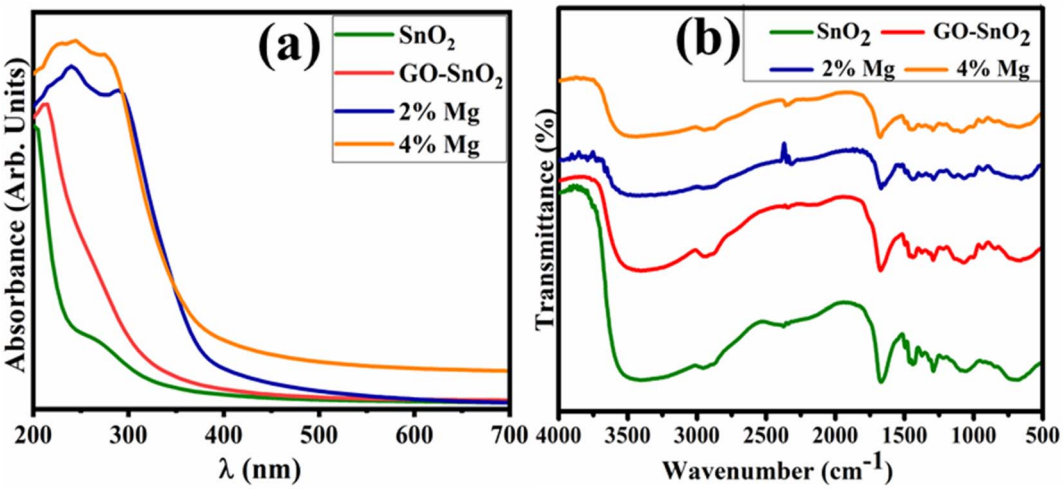

Fig. 3 (a) UV-vis spectra, (b) FTIR analysis of SnO_2, GO–SnO_2, 2% Mg/GO–SnO_2 and 4% Mg/GO–SnO_2.

The electronic structure of SnO_2 and Mg/GO–SnO_2 was characterized through UV-vis spectroscopy (Fig. 3a). SnO_2 showed absorption from 200 to 700 nm with a pronounced hump around 285 nm assigned to π–π* transition.[34] With Mg and GO, the absorption intensity of SnO_2 enhanced, introducing a redshift attributed to increased defect sites.[35] From the equation $E_g = 1240/\lambda_{onset}$,[36] the calculated E_g of SnO_2 decreased from 4.30 to 4.19 eV with the addition of GO and Mg.[33] The functional group identification of SnO_2 and Mg/GO–SnO_2 was analyzed utilizing FTIR analysis (Fig. 3b). The strong and broad bands at 3300–3500 and 1600–1640 cm^{-1} are attributed to –OH stretching and bending modes, respectively.[37] The bands ~1120–1381 cm^{-1} are attributed to Sn–OH bending vibration. The bands ~500–650 cm^{-1} correspond to O–Sn–O bending and Sn–O stretching modes, respectively.[38] With the addition of GO, variations in intensity and position were observed, caused by

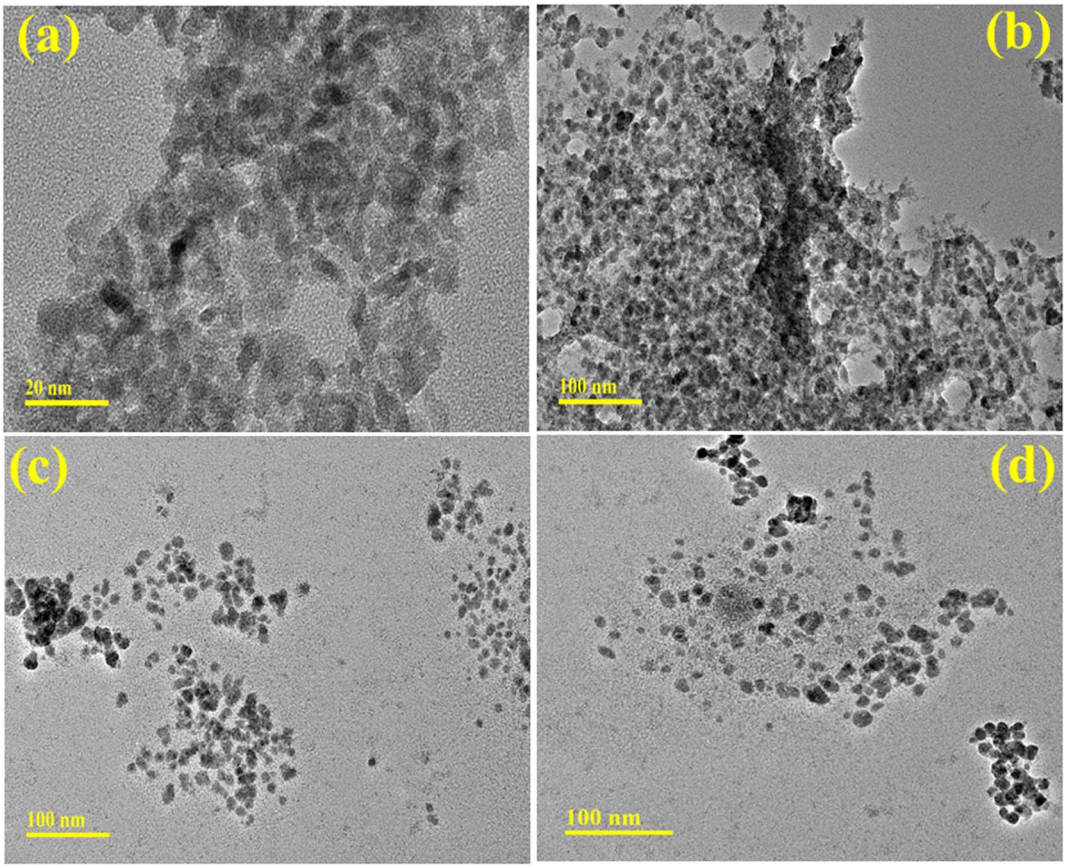

Fig. 4 (a–d) TEM analysis of (a) SnO_2[,[34] (b) GO–SnO_2, (c) 2% Mg/GO–SnO_2, and (d) 4% Mg/GO–SnO_2.

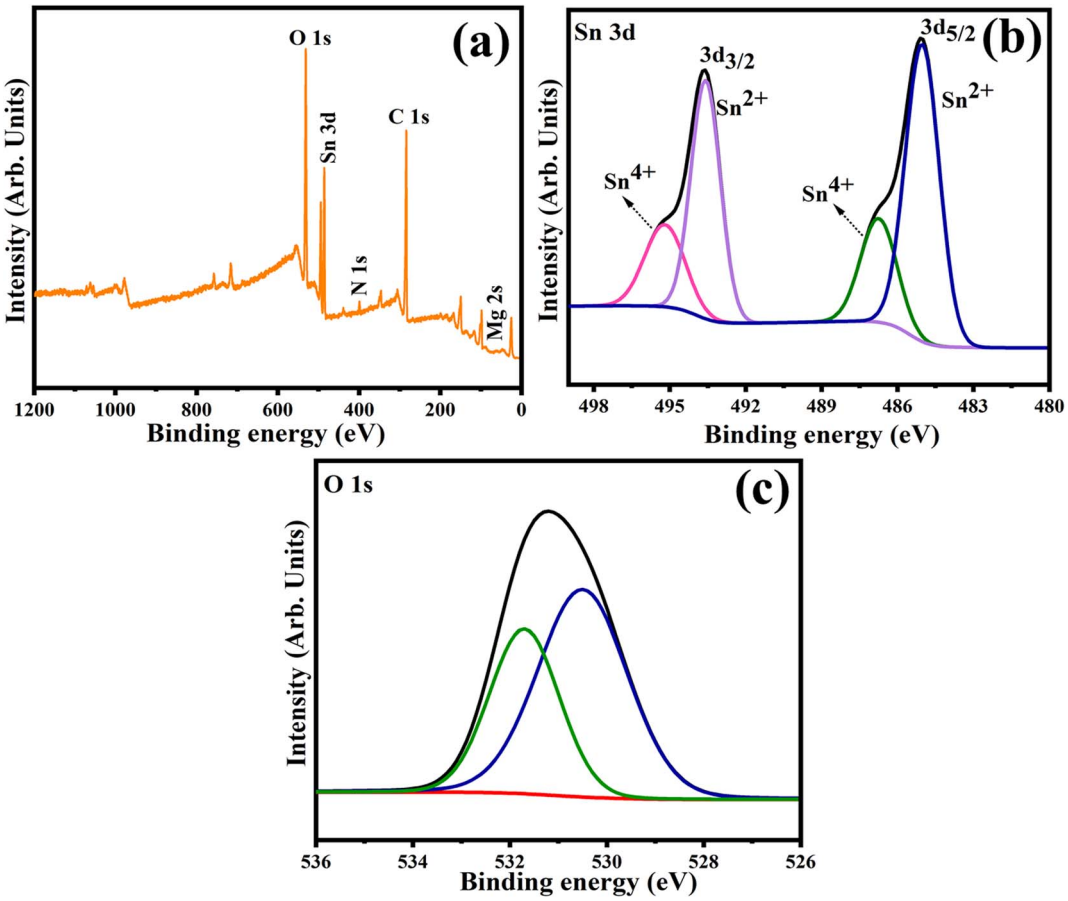

Fig. 5 (a) XPS survey spectrum of 4% Mg/GO–SnO_2 and the high-resolution spectra of (b) Sn 3d, and (c) O 1s.

the contribution of functional groups in GO–SnO_2.[39] The same trend was observed with Mg, possibly due to the introduction of Mg^{2+} into the SnO_2 crystal structure.[40]

EDS analysis characterized the elemental configuration of SnO_2 and Mg/GO-SnO_2 (Fig. S1a–d). Sn, O, C, and Mg peaks clarified the formation of Mg/GO–SnO_2. The Cl peak emerged as a result of using the precursor ($SnCl_2 \cdot 2HO$) in SnO_2 preparation. A Na peak appeared as NaOH was utilized during the synthesis process. Various concentrations of elements (Sn, O, C, Mg, and Na) *via* specific colors were analyzed through EDS mapping images (Fig. S1a′–d′).

The morphological properties of SnO_2 and Mg/GO–SnO_2 were characterized through TEM analysis (Fig. 4a–d). Fig. 4a demonstrates the non-uniform, randomly oriented, interconnected network of SnO_2 quantum dots with an average size of 4.55 nm measured through ImageJ software. With GO, overlapping and covering of nanosheets with interconnected QDs were observed (Fig. 4b). With 2% Mg, agglomeration decreased, and the same behavior was observed with a higher concentration (4%) of Mg (Fig. 4c and d).

To characterize the oxidation states of 4% of Mg doped GO–SnO_2, XPS analysis was utilized. Fig. 5a clarifies the presence of O 1s, Sn 3d, N 1s, C 1s, and Mg 2s. In the Sn 3d spectrum, peaks at 486.75 eV (Sn^{4+}) and 485.02 eV (Sn^{2+}) are ascribed to Sn $3d_{5/2}$ and peaks at 495.2 eV (Sn^{4+}) and 493.58 eV (Sn^{4+}) are attributed to Sn $3d_{3/2}$ (Fig. 5b).[41] In the high resolution O 1s spectrum, peaks at 530.5 eV (lattice oxygen bound to Sn) and 531.7 eV (oxygen deficient region in SnO_2) are observed, as shown in Fig. 5c.[42]

The degradation of RhB dye by prepared SnO_2 and Mg/GO–SnO_2 QDs was analyzed through a UV-vis spectrophotometer (absorption mode). The mechanism for the reduction of RhB

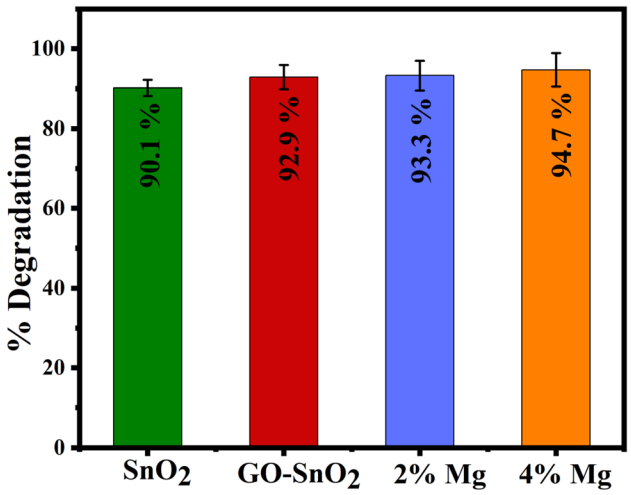

Fig. 6 Catalytic efficacy of SnO_2, GO–SnO_2, 2% Mg/GO–SnO_2, and 4% Mg/GO–SnO_2 in acidic medium.

was observed in the dark (absence of sunlight) and in the presence of synthesized catalysts (SnO_2 and Mg/GO–SnO_2) and a reducing agent ($NaBH_4$). During this process, prepared samples serve as an electron transfer medium, transferring e^- from $NaBH_4$ to the colored RhB dye (Fig. S2). The transfer of electrons to RhB causes the breakdown of the colored dye into less harmful compounds. SnO_2, GO–SnO_2, 2% Mg/GO–SnO_2, and 4% Mg/GO–SnO_2 showed 90.1, 92.9, 93.3, and 94.7% degradation efficacy in acidic medium, respectively (Fig. 6). The catalytic efficacy is a multidimensional process controlled by a variety of parameters such as size, dimension and surface area of the synthesized catalysts and pH of the catalyst medium. At pH 4, the immediate availability of H^+ ions protonated the surface, significantly enhancing the ionic interaction of RhB on the catalyst surface and demonstrating a high reduction of RhB.[28] Compared to SnO_2, GO–SnO_2 revealed improved catalytic efficiency, ascribed to π–π conjugation with the RhB chromophore group and high charge transfer efficacy.[43] With the dopants (Mg and GO), the catalytic efficacy is enhanced as the reduced size of SnO_2 leads to more active sites for dye reduction.

The antibacterial potential of SnO_2, GO–SnO_2, 2% Mg/GO–SnO_2, and 4% Mg/GO–SnO_2 was analyzed *in vitro* (Fig. S3), and the obtained outcomes are tabulated in Table 1. The inhibition zone diameters were found to be 0 ± 0.0 mm at 0.5 mg/50 μL (lowest concentration) and ranged from 1.85 ± 0.05–3.65 ± 0.03 mm at 1.0 mg/50 μL (highest concentration). The findings were contrasted with those of DI water (0 ± 0.0 mm) and ciprofloxacin, which exhibited a 6.85 ± 0.01 mm inhibitory zone. The optimized Mg/GO–SnO_2 demonstrated the highest antibacterial efficacy due to various synergistic processes. The catalyst likely facilitated the generation of reactive oxygen species (ROS), including hydroperoxyl radicals, hydroxyl radicals, superoxide anions, and hydrogen peroxide, which produced oxidative stress, damaging bacterial proteins and DNA ultimately leading to cell death. The 4% Mg/GO–SnO_2 QDs immobilized bacterial cells, inhibiting their multiplication, while the disruption of glycolysis impeded energy generation. Moreover, the liberation of metal ions interferes with bacterial enzymes and proteins. The combined effects lead to improved antibacterial effectiveness of 4% Mg/GO-SnO_2, the catalyst,

Table 1 Antibacterial efficacy of pure and Mg/GO-SnO_2 QDs

	Zone of inhibition (mm)	
Samples	500 μg/50 μL	1000 μg/50 μL
SnO_2	0 ± 0.0	1.85 ± 0.05
GO/SnO_2	0 ± 0.0	2.15 ± 0.04
2% Mg	0 ± 0.0	2.95 ± 0.04
4% Mg	0 ± 0.0	3.65 ± 0.03
Ciprofloxacin	6.85 ± 0.01	6.85 ± 0.01
DIW	0 ± 0.0	0 ± 0.0

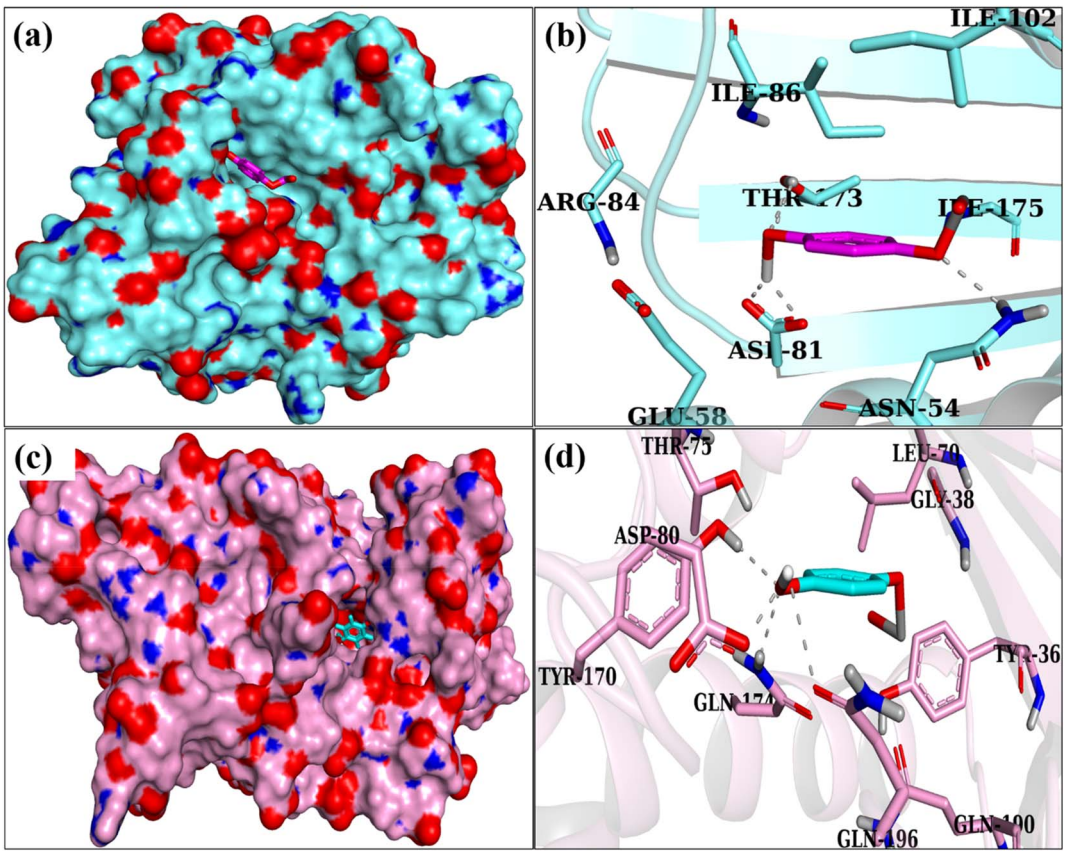

Fig. 7 The corresponding binding pockets (a and c) and binding interaction patterns (b and d) of Mg/GO-doped SnO_2 with active site residues of DNA gyrase and tyrosyl tRNA synthetase enzymes.

highlighting its promise for advantageous antimicrobial applications.[44–48]

The assessment of antioxidant activity of Mg/GO–SnO_2 was performed using DPPH free radical scavenging at 517 nm wavelength, with concentrations ranging from 25–125 μg mL^{-1} (Fig. S4). An improvement in scavenging efficacy is dependent on concentration, suggesting effective electron transfer. The 4% Mg-doped sample exhibited noteworthy antioxidant performance, attributed to increased availability of active sites and improved charge-transfer characteristics stemming from Mg integration, thus facilitating more efficient reduction of DPPH. The findings underscore the potential applications of QDs in the fields of biomedicine and therapeutic strategies.

In recent decades, molecular docking predictions have gained a lot of attention as a powerful tool for understanding different types of biological processes. There has been a lot of progress in recent years in identifying nanostructures with antibacterial capabilities, but there is still room for improvement in understanding the mechanisms that underlie these effects. The docking investigation of the DNA gyrase enzyme against *S. aureus* demonstrated that Mg/GO doped SnO_2 exhibited the most favorable configuration. Hydrogen bonding interactions were seen between Asn54, Gly85, and Thr173 in this conformation, leading to a binding score of 4.58 (Fig. 7a and b). Similar behavior was observed for the binding of Mg/GO doped SnO_2 into the active pocket of $TyrRS_{S.\ aureus}$, leading to an overall binding score of 4.51. Fig. 7c and d highlight the significant hydrogen bonding interactions between Asp80, Thr170, Gln174, and Gln196.

3.1 DFT and MESP studies

The electronic structures and reactivity of Mg/GO-doped SnO_2 in gaseous and solvent phases were clarified by DFT and MESP calculations using the B3LYP functional with the SVP basis set in Gaussian 09 (Rev. E.01) (Fig. 8a). The greatest electronegativity areas are indicated as deep red hue on MESP maps, highlighting regions for electrophilic and nucleophilic attacks on molecules. The oxygen atoms in Mg/GO-doped SnO_2 rings have Mulliken charges of −0.888036 and −0.836170, indicating a preponderance of negatively charged areas in respective aqueous and gas phases. The docking results indicate that proximity of oxygen atoms amplifies the capacity for hydrogen bonding in hinge and solvent-exposed areas of Mg/GO-doped SnO_2. The dominant green coloration on the Mg/GO-doped SnO_2 surface suggests an increased presence of neutral regions, potentially involved in van der Waals or hydrophobic interactions. The molecular surface depicted in Fig. 8b illustrates frontier orbitals, specifically the HOMO and LUMO for Mg/GO-doped SnO_2, which signify the molecule's capacity for effective electronic transitions, irrespective of increased chemical reactivity. The recorded energy gaps of Mg/GO-doped SnO_2 for gaseous and aqueous phases are 2.773 and 0.525 eV. The

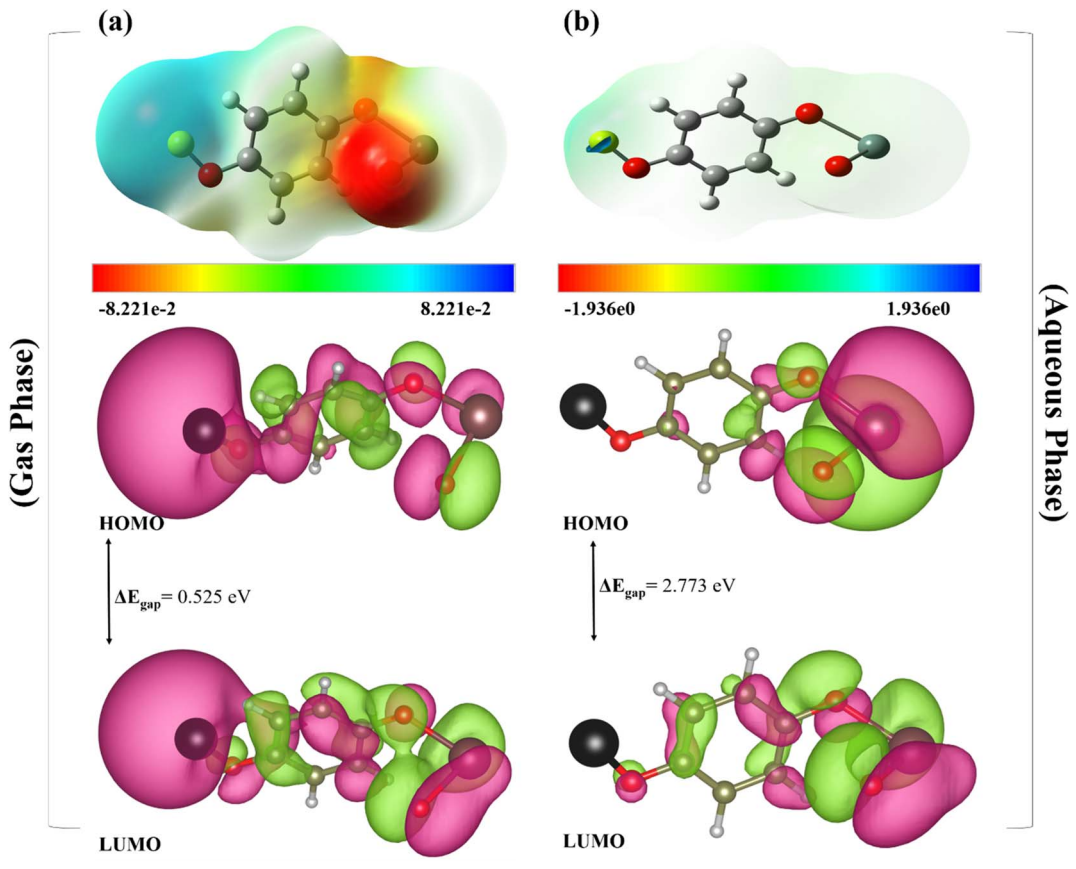

Fig. 8 MESP and HOMO–LUMO analysis of the selected ligand Mg/GO–doped SnO_2: (a) gas phase and (b) aqueous phase.

Table 2 DFT calculations (quantum chemical descriptors) of the selected ligands

Ligand	Dipole moment (Debye)	HOMO (a.u.)	LUMO (a.u.)	Energy gap (ΔE_{Gap})	Ionization potential (eV)	Electron affinity (eV)	Electronegativity χ (eV)	Electrochemical potential μ (eV)	Hardness η (eV)	Softness S (eV^{-1})	Electrophilicity ω (eV)
Mg/GO-doped SnO_2 (gas)	6.4896	−0.17464	−0.1553	0.52 eV	4.753	4.227	4.490	−4.490	0.263	3.802	38.34
Mg/GO-doped SnO_2 (aqueous)	32.5162	−0.15290	−0.0507	2.77 eV	4.162	1.387	2.775	−2.775	1.388	0.720	2.775

difference in energy between the two phases can be attributed to the influence of solvent. Within the aqueous environment, the polar solvent enhances the stabilization of molecular orbitals through dielectric screening, consequently augmenting the energy separation between these orbitals.

The solvent phase of Mg/GO-doped SnO_2 exhibited a dipole moment of 32.5162 debye, implying stable interactions, as outlined in Table 2. In conclusion, the aqueous phase exerts a stabilizing effect on the electronic structure, leading to wider energy gaps and moderated reactivity characteristics. This thorough electronic structure analysis explores structural attributes and functional performance, fostering exploration of nanostructures with enhanced therapeutic effectiveness.

4 Conclusion

SnO_2 and Mg/GO–SnO_2 QDs were effectively prepared for catalytic RhB reduction and bactericidal inactivation. XRD depicted the reduction in crystallinity with GO and Mg. UV-vis spectroscopy indicated increased absorption upon doping and a decreased E_g of SnO_2 from 4.30 to 4.19 eV. TEM analysis revealed multiple-shaped SnO_2 QDs and a decrease in QD size was observed with GO and Mg. The optimized Mg/GO–SnO_2 showed 94.7% RhB reduction in an acidic medium and similarly, a 3.65 ± 0.03 mm inhibition zone against MDR *S. aureus*. The results of molecular docking simulations exhibited concordance with the observed *in vitro* bactericidal effects against MDR *S. aureus*, indicating that the inhibition of DNA gyrase and TyrRS enzyme could potentially serve as a mechanism underlying the antibacterial properties of the unique Mg/GO doped SnO_2 nanocomposites. In summary, the optimized Mg/GO–SnO_2 synthesized through a co-precipitation approach exhibits greater potential as a catalyst for the reduction of RhB and the bactericidal inactivation of MDR *S. aureus*. The present research was conceived as a preliminary screening investigation; moreover, thorough evaluations based on MIC, alongside *in vivo* efficacy and cytotoxicity of the synthesized QDs are required in future.

Author contributions

Eman Rai – investigation, writing original draft, data curation, Muhammad Imran – conceptualization, supervision, methodology, Iram Shahzadi – software, writing original draft, formal analysis (computational study), Ali Haider – investigation, methodology (antibacterial part), Sawaira Moeen – writing review and editing, visualization, data curation, Anwar Ul-Hamid – resources, TEM investigation, I Boukhris – resources, writing review and editing, validation, Muhammad Ikram – conceptualization, funding acquisition, project administration, writing review and editing. The 1st author completed her research work under the supervision of 2nd author (currently in KFUPM).

Conflicts of interest

The authors declare no known conflict of interest.

Data availability

The data used in this manuscript can be made available upon reasonable request.

Supplementary information (SI) is available. See DOI: https://doi.org/10.1039/d5na00915d.

Acknowledgements

The authors are pleased to acknowledge higher education commission (HEC), Pakistan, for financial support through NRPU-20-17615 (Muhammad Ikram, PI).

References

1 N. M. Hosny, I. Gomaa and M. G. Elmahgary, Adsorption of polluted dyes from water by transition metal oxides: A review, *Appl. Surf. Sci. Adv.*, 2023, **15**, 100395.
2 T. Islam, *et al.*, Impact of textile dyes on health and ecosystem: a review of structure, causes, and potential solutions, *Environ. Sci. Pollut. Res.*, 2023, **30**(4), 9207–9242.
3 M. F. Mesleh, *et al.*, Fragment-based discovery of DNA gyrase inhibitors targeting the ATPase subunit of GyrB, *Bioorg. Med. Chem. Lett.*, 2016, **26**(4), 1314–1318.
4 O. Hamdaoui, Intensification of the sorption of Rhodamine B from aqueous phase by loquat seeds using ultrasound, *Desalination*, 2011, **271**(1–3), 279–286.
5 A. Depeursinge, *et al.*, Fusing visual and clinical information for lung tissue classification in high-resolution computed tomography, *Artif. Intell. Med.*, 2010, **50**(1), 13–21.
6 C. S. Zaragoza, *et al.*, Yeasts isolation from bovine mammary glands under different mastitis status in the Mexican High Plateu, *Rev. Iberoam. Micol.*, 2011, **28**(2), 79–82.
7 Z. Ilhan, *et al.*, Occurrence of fungal agents in mastitis in dairy goats, *J. Anim. Plant Sci.*, 2016, **29**(3), 4691–4700.
8 V. Krömker and S. Leimbach, Mastitis treatment—Reduction in antibiotic usage in dairy cows, *Reprod. Domest. Anim.*, 2017, **52**, 21–29.
9 R. Wahab, *et al.*, Antibacterial activity of ZnO nanoparticles prepared via non-hydrolytic solution route, *Appl. Microbiol. Biotechnol.*, 2010, **87**(5), 1917–1925.
10 M. F. Hanafi and N. Sapawe, Influence of pH on the photocatalytic degradation of methyl orange using nickel catalyst, *Mater. Today: Proc.*, 2020, **31**, 339–341.
11 J. Hassan, *et al.*, Application of chemically exfoliated boron nitride nanosheets doped with co to remove organic pollutants rapidly from textile water, *Nanoscale Res. Lett.*, 2020, **15**(1), 75.
12 S. Moeen, *et al.*, Comparative study of sonophotocatalytic, photocatalytic, and catalytic activities of magnesium and chitosan-doped tin oxide quantum dots, *ACS Omega*, 2022, **7**(50), 46428–46439.
13 U. T. Nakate, Y.-T. Yu and S. Park, Hydrothermal synthesis of ZnO nanoflakes composed of fine nanoparticles for H2S gas sensing application, *Ceram. Int.*, 2022, **48**(19), 28822–28829.
14 A. A. Mohammed, Z. T. Khodair and A. A. Khadom, Preparation and investigation of the structural properties of α-Al_2O_3 nanoparticles using the sol-gel method, *Chem. Data Collect.*, 2020, **29**, 100531.
15 K. Karthik, *et al.*, Ultrasound-assisted synthesis of V_2O_5 nanoparticles for photocatalytic and antibacterial studies, *Mater. Res. Innovations*, 2020, **24**(4), 229–234.
16 Z. Nasir, *et al.*, Co-precipitation synthesis and characterization of Co doped SnO_2 NPs, HSA interaction via various spectroscopic techniques and their antimicrobial and photocatalytic activities, *Int. J. Biol. Macromol.*, 2017, **94**, 554–565.
17 S. Steplinpaulselvin, R. Rajaram and I. Sharmila Lydia, Survival assessment of simple food webs for dye wastewater after photocatalytic degradation using SnO_2/GO nanocomposites under sunlight irradiation, *Sci. Total Environ.*, 2020, **721**, 137805.
18 D. J. Calderón, *et al.*, Effect of synthesis variables on the characteristics of magnesium hydroxide nanoparticles and evaluation of the fluorescence of functionalised Mg $(OH)_2$ nanoparticles, *Adv. Nat. Sci.:Nanosci. Nanotechnol.*, 2020, **11**(2), 025008.
19 C. Ngnintedem Yonti, *et al.*, Green synthesis of iron-doped cobalt oxide nanoparticles from palm kernel oil via co-precipitation and structural characterization, *Nanomaterials*, 2021, **11**(11), 2833.
20 K. Kaviyarasu, *et al.*, Solution processing of CuSe quantum dots: Photocatalytic activity under RhB for UV and visible-light solar irradiation, *Mater. Sci. Eng., B*, 2016, **210**, 1–9.
21 C. Nayral, *et al.*, Synthesis and use of a novel SnO2 nanomaterial for gas sensing, *Appl. Surf. Sci.*, 2000, **164**(1–4), 219–226.
22 L. Cojocaru, *et al.*, Size and shape fine-tuning of SnO_2 nanoparticles for highly efficient and stable dye-sensitized solar cells, *J. Mater. Chem. A*, 2013, **1**(44), 13789–13799.
23 F. M. Courtel, *et al.*, In situ polyol-assisted synthesis of nano-SnO_2/carbon composite materials as anodes for lithium-ion batteries, *J. Power Sources*, 2010, **195**(8), 2355–2361.
24 Y. Zhang, *et al.*, Growth of 3D SnO_2 nanosheets on carbon cloth as a binder-free electrode for supercapacitors, *J. Mater. Chem. A*, 2015, **3**(29), 15057–15067.
25 S. Pan, *et al.*, Surface Fe^{3+}-decorated pristine SnO_2 nanoparticles with enhanced· OH radical generation performance, *Catal. Commun.*, 2012, **24**, 96–99.
26 F. Wang, *et al.*, SnO_2/Graphene Nanocomposite Coated by Carbonized Polyacrylic Acid Hydrogel as a High-Performance Anode for Lithium-Ion Batteries, *ChemistrySelect*, 2019, **4**(27), 8082–8088.
27 T. Munawar, *et al.*, Transition metal-doped SnO_2 and graphene oxide (GO) supported nanocomposites as efficient photocatalysts and antibacterial agents, *Environ. Sci. Pollut. Res.*, 2022, **29**(60), 90995–91016.
28 S. Riaz, *et al.*, Bactericidal action and industrial dye degradation of graphene oxide and polyacrylic acid-doped SnO2 quantum dots: In silico molecular docking study, *ACS Omega*, 2023, **8**(6), 5808–5819.
29 M. Khan, *et al.*, Experimental and DFT study of GO-decorated CaO quantum dots for catalytic dye degradation

and bactericidal potential, *Front. Environ. Sci.*, 2023, **11**, 1158399.
30 X. Qiu, *et al.*, Crystal structure of Staphylococcus aureus tyrosyl-tRNA synthetase in complex with a class of potent and specific inhibitors, *Protein Sci.*, 2001, **10**(10), 2008–2016.
31 I. Shahzadi, *et al.*, Formation of biocompatible MgO/cellulose grafted hydrogel for efficient bactericidal and controlled release of doxorubicin, *Int. J. Biol. Macromol.*, 2022, **220**, 1277–1286.
32 C. Fu, *et al.*, Evaluation and characterization of reduced graphene oxide nanosheets as anode materials for lithium-ion batteries, *Int. J. Electrochem. Sci.*, 2013, **8**(5), 6269–6280.
33 V. Perumal, *et al.*, Hierarchical nanorods of graphene oxide decorated SnO_2 with high photocatalytic performance for energy conversion applications, *Fuel*, 2022, **324**, 124599.
34 A. Habib, *et al.*, Experimental and theoretical study of catalytic dye degradation and bactericidal potential of multiple phase Bi and MoS_2 doped SnO_2 quantum dots, *RSC Adv.*, 2023, **13**(16), 10861–10872.
35 S. Jian, *et al.*, Enhanced visible light photocatalytic efficiency of La-doped ZnO nanofibers via electrospinning-calcination technology, *Adv. Powder Mater.*, 2022, **1**(2), 100004.
36 T. M. H. Nguyen and C. W. Bark, Synthesis of cobalt-doped TiO_2 based on metal–organic frameworks as an effective electron transport material in perovskite solar cells, *ACS Omega*, 2020, **5**(5), 2280–2286.
37 W. Raza, *et al.*, Synthesis, characterization and photocatalytic performance of visible light induced bismuth oxide nanoparticle, *J. Alloys Compd.*, 2015, **648**, 641–650.
38 K. Suresh, *et al.*, Green synthesis of SnO_2 nanoparticles using Delonix elata leaf extract: Evaluation of its structural, optical, morphological and photocatalytic properties, *SN Appl. Sci.*, 2020, **2**(10), 1735.
39 I. Boukhoubza, *et al.*, Graphene oxide concentration effect on the optoelectronic properties of ZnO/GO nanocomposites, *Nanomaterials*, 2020, **10**(8), 1532.
40 V. Etacheri, R. Roshan and V. Kumar, Mg-doped ZnO nanoparticles for efficient sunlight-driven photocatalysis, *ACS Appl. Mater. Interfaces*, 2012, **4**(5), 2717–2725.
41 A. d. O. Jorgetto, M. V. Boldrin Zanoni and M. O. Orlandi, Assessment of the superior photocatalytic properties of Sn^{2+}-containing SnO_2 microrods on the photodegradation of methyl orange, *Sci. Rep.*, 2023, **13**(1), 14774.
42 M. Kumar, *et al.*, New insights towards strikingly improved room temperature ethanol sensing properties of p-type Ce-doped SnO_2 sensors, *Sci. Rep.*, 2018, **8**(1), 8079.
43 T. V. M. Sreekanth, M.-J. Jung and I.-Y. Eom, Green synthesis of silver nanoparticles, decorated on graphene oxide nanosheets and their catalytic activity, *Appl. Surf. Sci.*, 2016, **361**, 102–106.
44 Y. Anwar, *et al.*, Antibacterial and lead ions adsorption characteristics of chitosan-manganese dioxide bionanocomposite, *Int. J. Biol. Macromol.*, 2018, **111**, 1140–1145.
45 T. Dutta, *et al.*, ROS generation by reduced graphene oxide (rGO) induced by visible light showing antibacterial activity: comparison with graphene oxide (GO), *RSC Adv.*, 2015, **5**(98), 80192–80195.
46 S. M. Amininezhad, *et al.*, The antibacterial activity of SnO_2 nanoparticles against Escherichia coli and Staphylococcus aureus., *Zahedan J. Res. Med. Sci.*, 2015, **17**(9), 5307–5315.
47 V. Lakshmi Prasanna and R. Vijayaraghavan, Insight into the mechanism of antibacterial activity of ZnO: surface defects mediated reactive oxygen species even in the dark, *Langmuir*, 2015, **31**(33), 9155–9162.
48 G. Asnag, A. Oraby and A. Abdelghany, Effect of gamma-irradiation on the structural, optical and electrical properties of PEO/starch blend containing different concentrations of gold nanoparticles, *Radiat. Eff. Defects Solids*, 2019, **174**(7–8), 579–595.

